J. Fluid Mech. (2006), *vol.* 563, *pp.* 71–80. © 2006 Cambridge University Press
doi:10.1017/S0022112006000851 Printed in the United Kingdom

The rolling up of sheets in a steady flow

By LIONEL SCHOUVEILER[1] AND AREZKI BOUDAOUD[2]

[1]Institut de Recherche sur les Phénomènes Hors Équilibre, 49 rue Joliot-Curie, BP 146, F-13384 Marseille Cedex 13, France

[2]Laboratoire de Physique Statistique, Ecole Normale Supérieure, 24 rue Lhomond, F-75231 Paris Cedex 05, France

(Received 21 January 2006 and in revised form 9 May 2006)

The mechanism of reconfiguration of broad leaves subjected to wind loading is investigated. Circular plastic sheets cut along a radius are immersed in a water flow. They roll up into cones when held at their centres. The opening angle of the cone and the drag force exerted on the sheet are measured as a function of the flow velocity and of the sheet bending rigidity. The cone becomes sharper when the velocity increases or when the sheet stiffness decreases; the reconfiguration leads to a decrease in the drag coefficient. Scaling laws are derived from the mechanical equilibrium of the sheets – the balance between form drag and elastic forces – and the experimental data collapse onto master curves. Two models for the pressure field yield theoretical curves in semi-quantitative agreement with the experiments.

1. Introduction

To withstand high wind loads without damage, plants have developed different strategies. For instance, for broad-leaved species such as the tuliptree or red maple, Vogel (1989) reports the shape reconfiguration of the leaves into cones. This gives rise to a streamlining of the leaf and a reduction of the surface area exposed to the wind, and results in a reduction of the drag coefficient with increasing wind speed. A review of the corresponding biomechanical constraints is given by Niklas (1999). One might wonder whether physiological processes are involved or the coupling between the flow and a flexible object suffices to cause reconfiguration. This was one of the motivations of Alben, Shelley & Zhang (2002, 2004) who performed two-dimensional experiments on the deformation of a flexible fibre held in a flowing soap film. They observed the fibre to bend as the velocity of the flow was increased and found the drag coefficient to vanish at high velocity. They solved the corresponding coupled elastic–fluid problem and obtained a quantitative agreement with the experiments. However, as the behaviour of slender elastic objects depends strongly on their dimensionality (see e.g. Landau & Lifchitz 1990), we aim here to extend the investigations of Alben *et al.* (2002, 2004) to a more realistic three-dimensional configuration.

Although fluid–structure interactions have received much attention, most studies were restricted to small deformations of the elastic structure, often aimed at characterizing its stability, vibrations or sound emission (Howe 1998). This might be due to the lack of analytical methods or to the requirement of highly sophisticated numerical methods (see Etienne & Pelletier 2005, and references therein) in order to couple large elastic deformations with a flow. Schouveiler, Eloy & Le Gal (2005)

https://doi.org/10.1017/S0022112006000851 Published online by Cambridge University Press

also investigated experimentally and theoretically the equilibrium shapes of a flexible filament hanging in a flow, having therefore large deformations. In practice, most structures are stiff enough not to be deformed by a flow. The notable exception comes from sailing: the shape of sails in an airflow has been the subject of numerous studies (for a review, see Lorillu, Weber & Hureau 2002), although the elasticity of the sail was usually neglected.

The present study concerns the deformation of elastic sheets put into a flow and is motivated by the observations of Vogel (1989) on tree leaves. The leaf reconfiguration by flow-induced forces is first experimentally reproduced in the laboratory using plastic sheets in a water channel. Section 2 reports on these experiments. In § 3 we formulate the coupled elastic and hydrodynamic problem and we give two models for the pressure field. Theoretical and experimental results are compared and analysed in § 4 before the concluding discussion of § 5.

2. Experiments

We considered a thin circular plastic sheet, of radius R and bending rigidity D, cut along one radius. It was held in a water flow of velocity U perpendicular to the initial sheet. Experiments were conducted in a free-surface water channel. The test section was 140 cm long with a water depth at rest of 45 cm and was slightly diverging to compensate for the downstream growth of the boundary layers on the tunnel walls. The width of the section that initially contained the sheet was 38 cm. The free-stream velocity U could be continuously varied up to $1\,\mathrm{m\,s^{-1}}$. The sheets were held at their centre in the channel, at the end of an upstream tube parallel to the flow. The tube was rigidly attached perpendicularly to a beam that was fixed on a frame above the free surface.

Eleven sheets were tested: five of radius $R = 10\,\mathrm{cm}$ and of different bending rigidities D ranging from 0.27×10^{-3} to $3.03 \times 10^{-3}\,\mathrm{N\,m}$, and seven of bending rigidity $D = 0.99 \times 10^{-3}\,\mathrm{N\,m}$ and of radii R ranging from 4 to 10 cm. We used plastic sheets such as transparencies or plastic covers. For each type of sheet, the rigidity D was deduced from the measurement of the small deflections due to gravity of a strip clamped at one end, when varying the strip length.

Without a flow ($U = 0$) the sheet was flat and perpendicular to the channel section. When subjected to the flow load, the sheet rolled up into a cone with a circular base. The ratio of the plastic to the water density being close to 1, the apparent weight of the sheet was negligible and the cone appeared symmetric around an axis parallel to the incoming flow. The cone became increasingly acute as the flow speed was increased. The flow-induced reconfiguration is illustrated in figure 1 for a sheet of radius $R = 10\,\mathrm{cm}$ and bending rigidity $D = 0.27 \times 10^{-3}\,\mathrm{N\,m}$ at three different values of U. Photographs were taken using a monochrome video camera, perpendicularly to the flow, through the glass sidewall of the channel.

The sheet reconfiguration was quantified using the opening angle of the cone α, as defined in figure 1(a) so that $\alpha = 0$ when the sheet is flat ($U = 0$). We actually measured the vertex angle 2ϵ between the two lines that limit the cone on the visualizations and deduced $\alpha = \pi/2 - \epsilon$. The evolution of α with the flow velocity U is shown in figure 2 for the eleven sheets tested. As U is increased from 0, α smoothly increases with a rate that becomes weaker and weaker. Figure 2(a) shows the effect of varying the bending rigidity D. As expected, the angle α decreases as the bending rigidity D is increased. For the two most flexible sheets ($D = 0.27 \times 10^{-3}$ and $0.59 \times 10^{-3}\,\mathrm{N\,m}$), α is not defined for the highest velocities because then the axisymmetry is lost with the

https://doi.org/10.1017/S0022112006000851 Published online by Cambridge University Press

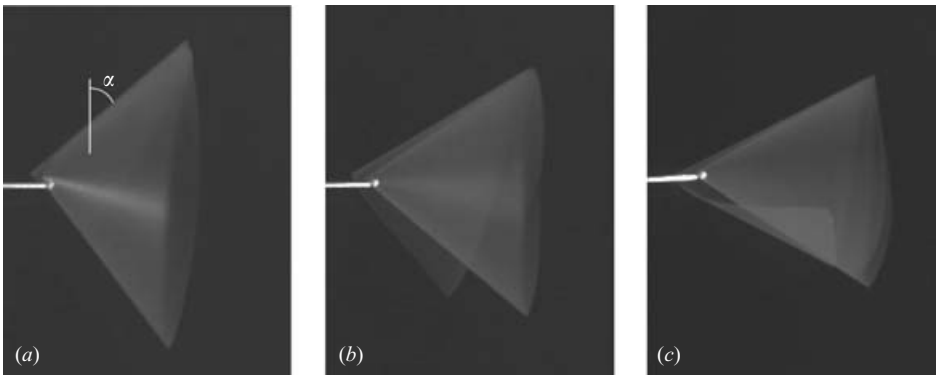


FIGURE 1. Visualizations of the sheet reconfiguration into increasingly sharp cones for a sheet of bending rigidity $D = 0.27 \times 10^{-3}$ N m and radius $R = 10$ cm: (*a*) $U = 8.3$ cm s^{-1}, (*b*) 17.7 cm s^{-1}, (*c*) 59.1 cm s^{-1}. Flow from left to right. The cone opening angle α is defined in (*a*).

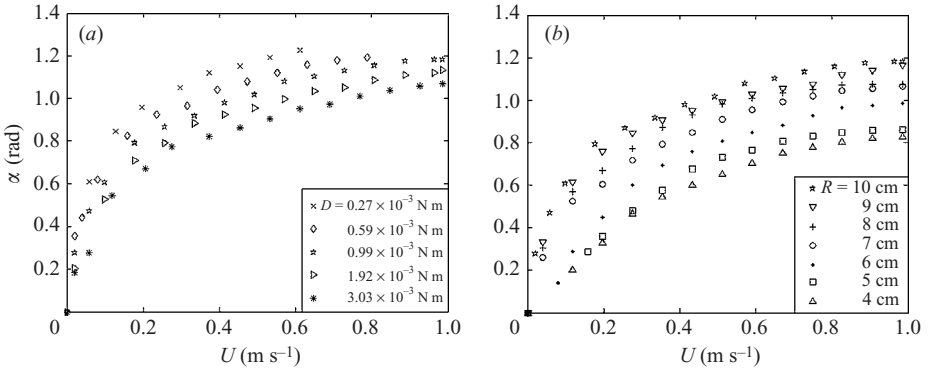


FIGURE 2. Bending angle α as a function of the free-stream velocity U: effects of (*a*) bending rigidity D for $R = 10$ cm and (*b*) of sheet radius R for $D = 0.99 \times 10^{-3}$ N m.

appearance of two folds along the cone. Similarly, figure 2(*b*) shows the evolution of α for a given rigidity and different radii R. α appears to be a decreasing function of R: the reconfiguration is more important for the largest sheets. It should be pointed out that here U is the free-stream velocity; in fact the flow velocity continuously increases from the tip along the cone because of the continuous section reduction.

In order to measure the drag force d acting on sheets, the support beam was attached to a four-strain-gauge calibrated balance (DeltaLab EI 450). Results for sheets of radius $R = 10$ cm and of two different bending rigidities are shown in figure 3 together with data that we obtained for a rigid disk of the same radius and held perpendicularly to the free stream. For these data, the drag exerted on the support alone was measured and subtracted from the total drag measured with the sheets. While for the rigid disk we find the classical quadratic behaviour (shown by the U^2 fit curve in figure 3, which incidentally indicates that the viscous drag is negligible in this velocity range), the comparison with the data for flexible sheets shows that the flow-induced reconfiguration allows the leaves to strongly reduce the load they have to sustain. This optimization is more important as the rigidity becomes smaller due to the smaller area exposed to the flow.

https://doi.org/10.1017/S0022112006000851 Published online by Cambridge University Press

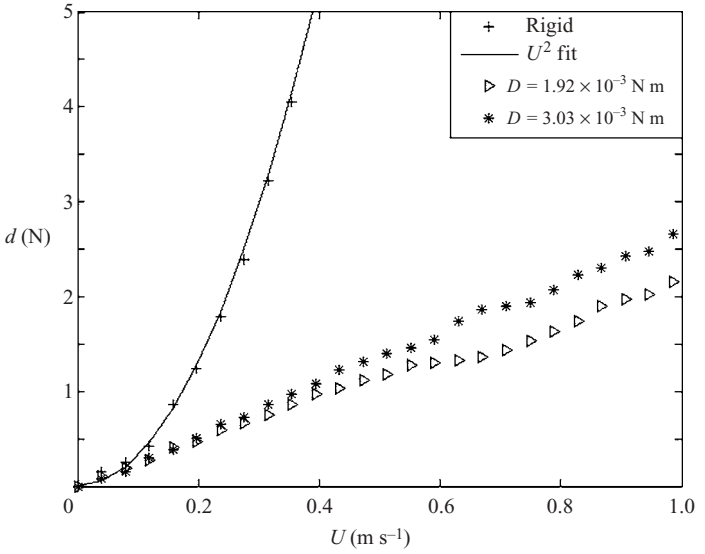


FIGURE 3. Drag force d as a function of the free-stream velocity U for two sheets of radius $R = 10$ cm, and comparison with the drag on a rigid disk of the same radius.

3. Theory

3.1. *Formulation*

We consider here the static equilibrium of a circular sheet of bending rigidity D and of radius R. It is cut along one radius and its centre is fixed in a steady flow of free-stream velocity U. To express our theoretical model, we use the spherical coordinate system with origin at the sheet centre and axis of reference given by the direction of the flow, r being the polar distance, θ the azimuthal angle and ϕ the polar angle. In general, a sheet has two modes of deformation: bending – the sheet acquires a curvature – and stretching – distances on the sheet are changed. First, let us note that, as the sheet is thin, pure bending deformations are preferred here as they are allowed by the boundary conditions (see e.g. Rayleigh 1945). So we consider only bending of the sheet. Furthermore, in agreement with the experimental observations we assume that the system keeps a symmetry of revolution. Pure bending deformations of a surface with a symmetry of revolution yield only cylinders and cones. Here the sheet is held at its centre so that it should have the shape of a cone of opening angle α (as defined in figure 1*a*). Let $P_\alpha(r)$ be the differential dynamic pressure field exerted by the flow on such a cone, i.e. the difference between the pressures on the upward and leeward sides of the sheet. The energy of the sheet is the sum of its elastic bending energy due to a curvature $c(r)$ and of the potential energy due to the flow pressure:

$$\mathscr{E} = \frac{1}{2} D \int_S c^2 \, \mathrm{d}S - \int_0^\alpha \mathrm{d}\alpha' \int_{S_{\alpha'}} P_{\alpha'} r \, \mathrm{d}S_{\alpha'}, \tag{3.1}$$

where the first integral is calculated over all the sheet surface $S = \pi R^2$ whereas the second term contains the total pressure torque over the surface exposed to the incoming flow $S_{\alpha'} = \pi R^2 \cos\alpha'$. Note that because the ratio of the sheet material density to the fluid density is close to one and because we consider values of the Reynolds number Re ($Re = UR/\nu$ compares inertia and viscous forces, ν being the kinematical viscosity of the fluid) as large as 10^5, any gravity and viscous effects are neglected.

https://doi.org/10.1017/S0022112006000851 Published online by Cambridge University Press

The local curvature of a cone of opening angle α being given by

$$c = \tan\alpha / r, \tag{3.2}$$

the first integral in (3.1) appears to be logarithmically divergent as r goes to 0, so that a cut-off radius R_c is needed. Experimentally this cut-off corresponds to the size of the holding tube $R_c \simeq 1\,\mathrm{mm}$; its precise value is unimportant because the dependence of $\mathscr{E}$ on R_c is only logarithmic. Introducing the non-dimensional pressure $\tilde{P}_\alpha(\tilde{r}) = P_\alpha(R\tilde{r})/(\rho U^2)$, where ρ is the fluid density, and using the radius of the sheet R as a unit of length, the total potential energy $\mathscr{E}$ (3.1) becomes

$$\mathscr{E} = \pi D \ln\left(\frac{R}{R_c}\right)\tan^2\alpha - \rho U^2 R^3 \int_0^\alpha \mathrm{d}\alpha' \int_{\tilde{r}=0}^{\tilde{r}=1} \tilde{P}_{\alpha'}(\tilde{r})\tilde{r}\; 2\pi\tilde{r}\cos\alpha'\,\mathrm{d}\tilde{r}. \tag{3.3}$$

The ratio between the two energy scales is the elastohydrodynamical number

$$\mathscr{N} = \frac{\rho U^2 R^3}{D\ln(R/R_c)} = \left(\frac{U}{U_c}\right)^2. \tag{3.4}$$

Then finding the cone equilibrium angle reduces to finding the minimum of the reduced energy $\tilde{\mathscr{E}}(\alpha) = \mathscr{E}(\alpha)/(2\pi D\ln(R/R_c))$, i.e. the zeros of

$$\frac{\partial\tilde{\mathscr{E}}}{\partial\alpha} = \frac{\sin\alpha}{\cos^3\alpha} - 2\mathscr{N}\int_{\tilde{r}=0}^{\tilde{r}=1}\tilde{P}_\alpha(\tilde{r})\tilde{r}^2\cos\alpha\,\mathrm{d}\tilde{r}. \tag{3.5}$$

However the pressure field is still unknown at this stage and is the subject of the following subsection.

3.2. *A model for the pressure field*

Alben *et al.* (2002, 2004) used Helmholtz's free-streamline theory to compute the pressure field around their flexible fibre held in a flowing soap film. This method relies heavily on complex variables which restricts it to two dimensions. Unfortunately, we are not aware of any analytical or semi-analytical method for three-dimensional problems. Thus our primary goal is to provide a qualitative understanding of the experiments.

3.2.1. *A potential flow model*

Instead of looking for a potential flow with the correct boundary conditions at infinity and modelling the separation at the edge of the cone, we assume that the local form of the velocity potential at the tip holds all over the cone, imposing that the velocity at the edge ($r = R, \theta = \pi/2 + \alpha$) is equal to the far-field velocity U.

A separable solution to Laplace's equation is

$$\psi(r,\theta) = \psi_0 r^n L(n, \cos\theta), \tag{3.6}$$

L being a Legendre function of the first kind. The corresponding velocity field is

$$u_r = n\psi_0 r^{n-1} L(n,\cos\theta), \tag{3.7}$$

$$u_\theta = \psi_0 r^{n-1}(\cos\theta\, L(n,\cos\theta) - L(n-1,\cos\theta))/\sin\theta. \tag{3.8}$$

The kinematic boundary condition at the cone surface

$$u_\theta(r, \theta = \pi/2 + \alpha) = 0 \tag{3.9}$$

determines the value of the exponent n as a function of α (choosing the smallest value of n such that there is no divergence of the velocity field). This $n(\alpha)$ yields the self-similar behaviour of any velocity potential near a cone tip.

https://doi.org/10.1017/S0022112006000851 Published online by Cambridge University Press

We assume that this form holds even far from the tip and we try to 'match' it to the far-field velocity by imposing that

$$u_r(r = R, \theta = \pi/2 + \alpha) = U, \tag{3.10}$$

which determines the prefactor ψ_0 of the velocity potential. This condition amounts to stating that the pressure in the wake p_w is equal to the far-field pressure p_∞ (see below).

In order to determine the differential pressure P_α exerted on the sheet, we use Bernouilli's equation, the pressure on the windward side being $p_w + P_\alpha$,

$$p_w + P_\alpha(r) + \tfrac{1}{2}\rho u_r^2 = p_\infty + \tfrac{1}{2}\rho U^2. \tag{3.11}$$

Again under the assumption that $p_w = p_\infty$, we obtain the non-dimensional form

$$\tilde{P}_\alpha(\tilde{r}) = \tfrac{1}{2}\left(1 - \tilde{r}^{2n(\alpha)-2}\right), \tag{3.12}$$

n being determined by the implicit equation (3.9). Note that this assumption on the leeward pressure amounts to neglecting the recirculation flow behind the cone.

Plugging relation (3.12) into the equilibrium condition given by (3.5) allows the equilibrium angle α to be calculated according to the potential flow model. Note that this model is an approximation in the sense that the expansion of the velocity potential is truncated at its lower power in r.

3.2.2. *A momentum conservation model*

A simpler expression for the pressure field can be obtained using a momentum flux balance. If we assume that the drag d on the sheet is generated by the deviation of a section of area $S = \pi R^2 \cos^2\alpha$ (equal to the area of the base of the cone) of the upward flow (momentum flux ρv^2) by an angle α, we find that

$$d = \rho v^2 (1 - \sin\alpha)\pi R^2 \cos^2\alpha. \tag{3.13}$$

If we moreover assume that the pressure field is constant over the cone then we obtain

$$P_\alpha(r) = \rho v^2 (1 - \sin\alpha), \tag{3.14}$$

or in non-dimensional terms

$$\tilde{P}_\alpha(\tilde{r}) = 1 - \sin\alpha. \tag{3.15}$$

This formula yields the equilibrium angle α according to the momentum conservation model.

According to this model, the present system would be equivalent to the problem of a cone in a free jet, the cross-section of which was arbitrarily chosen as equal to the cone basis. Also, assuming the pressure field to be constant on the cone is not very realistic; however the results of both models appear very similar (see below). This might be ascribed to the fact that the equilibrium angle does not depend on the details of the pressure field but only on an integral.

4. Results

4.1. *Drag on a cone*

As a check and to compare with known results on the drag on a cone, we computed the drag coefficient on a cone as resulting from our two pressure fields:

$$C = \frac{d}{\frac{1}{2}\rho U^2 \pi R^2 \cos^2\alpha},$$

https://doi.org/10.1017/S0022112006000851 Published online by Cambridge University Press

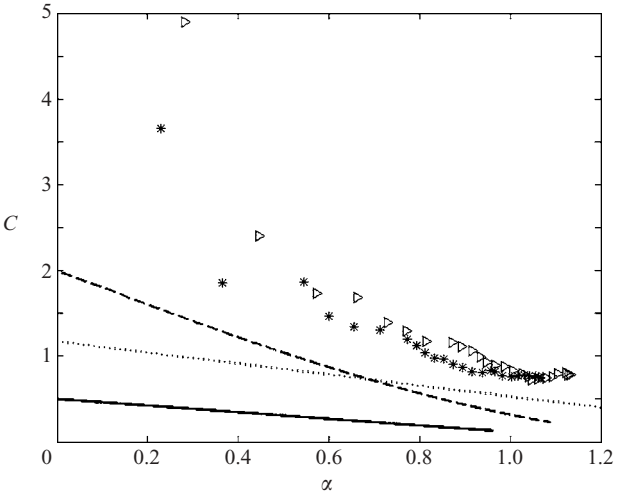


FIGURE 4. Drag coefficient C versus cone angle α: experimental data (same symbols as in figure 3), the linear fit of Hoerner's data ($\cdots$) and theoretical curves as deduced from the potential flow model (—) and from the momentum conservation model (- - -).

where the surface of reference is the base of the cone and the drag force is given by

$$d = \int_{S_\alpha} P_\alpha(r) \cos\alpha \, \mathrm{d}S_\alpha. \tag{4.1}$$

For the potential flow model, we find $C = 1 - 1/n(\alpha)$ which decreases from $1/2$ for $\alpha = 0$ to 0 for $\alpha = \pi/2$. For the momentum conservation model, $C = 2(1 - \sin\alpha)$ which decreases from 2 for $\alpha = 0$ to 0 for $\alpha = \pi/2$. In the experimental data given by Hoerner (1993), the drag coefficient decreases from 1.17 ($\alpha = 0$) to 0.16 ($\alpha = \pi/2$). Figure 4 shows these results, along with the experimental measurements for the drag coefficient. It should be pointed that the lower values of the angle α (< 0.4) correspond to a Reynolds number in the range 500–1000, so that they are directly comparable neither to the two inviscid theories nor to Hoerner's data (Reynolds number of the order of 10^4), because of the contribution of the viscous drag. Except for small angles, all the curves have the same trends; our measurements are higher than Hoerner's by roughly 50 %. However Hoerner warns that his data should be corrected using the value of the pressure in the wake and our measurements imply the existence of a more negative dynamic pressure in the wake. The most likely explanation is that the detachment at the trailing edge of hollow cones (the present study) differs from the case of the full cones of Hoerner (1993) as this is the main difference between the two experimental systems.

4.2. *The equilibrium angle*

In the model presented above, the equilibrium angle α is assumed to result from a balance between flow pressure on the sheet and sheet rigidity; this leads to a characteristic velocity scale U_c and to the natural elastohydrodynamical control parameter $\mathcal{N} = (U/U_c)^2$. In spite of its simplicity, this scaling analysis is confirmed by our experimental observations: figure 5 shows that the experimental values of the angle α for the eleven tested sheets collapse on a single curve when they are plotted with respect to the non-dimensional parameter $\mathcal{N}$. Dispersion appears to be more important for small $\mathcal{N}$, which might be ascribed to the viscous drag which was

https://doi.org/10.1017/S0022112006000851 Published online by Cambridge University Press

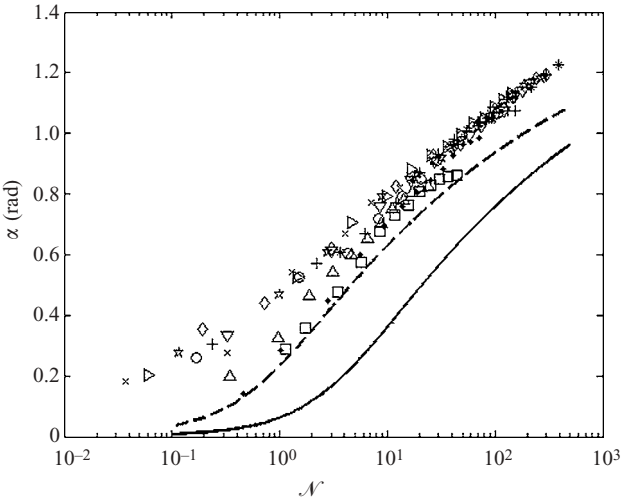


FIGURE 5. Angle α versus the non-dimensional elastohydrodynamical number $\mathcal{N}$: experimental data (same symbols as in figure 2) and theoretical curves as deduced from the potential flow model (—) and from the momentum conservation model (- - -).

neglected in the analysis. The two theoretical curves, deduced from the potential flow model and from the momentum conservation model, are also plotted in figure 5. They evolve smoothly from $\alpha = 0$ to the limiting value $\alpha = \pi/2$. Although both theories have a tendency to underestimate the experimental data, the qualitative description of the evolution of the opening angle is good and quantitatively not very far from the experimental values. Figure 5 seems to indicate that the momentum conservation model is more relevant than the potential one. But it should be pointed out that the data corresponding to this model in figure 5 have been calculated for a jet section arbitrarily chosen as equal to the cone base. In this sense, this section can be seen as a adjustment parameter for the experimental data.

4.3. *The drag coefficient*

As we are interested in the drag reduction through folding, we define the drag coefficient

$$C_d = \frac{d}{\frac{1}{2}\rho U^2 \pi R^2}, \tag{4.2}$$

using the initial sheet area πR^2 as a reference.

We find that

$$C_d = (1 - 1/n(\alpha)) \cos^2 \alpha, \tag{4.3}$$

for the potential flow model and

$$C_d = 2(1 - \sin \alpha) \cos^2 \alpha \tag{4.4}$$

for the momentum conservation model.

The drag coefficient evolution with respect to the non-dimensional parameter $\mathcal{N}$ is shown in figure 6. The experimental C_d have been calculated using (4.2) with the measured drag values d of figure 3; we note that, as for the angle α (see figure 5), the points for the two tested sheets fall on a single curve when plotted versus $\mathcal{N}$. Moreover, and in contrast to the rigid disk, for which we have seen in figure 3 that the drag is proportional to U^2 (that is the drag coefficient is constant), for the flexible

https://doi.org/10.1017/S0022112006000851 Published online by Cambridge University Press

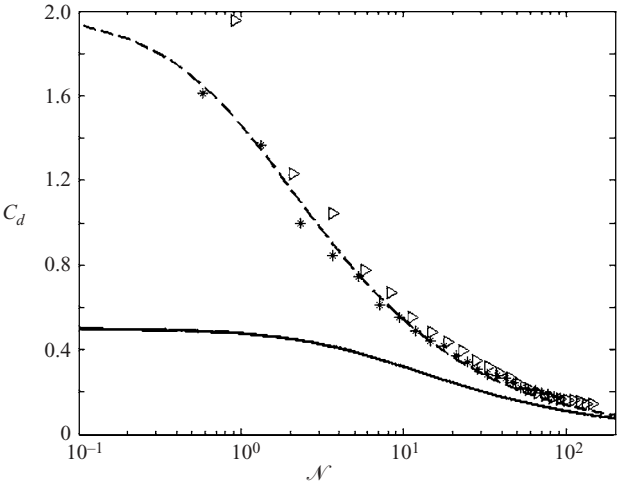


FIGURE 6. Drag coefficient C_d (defined with the area of the flat sheet) versus the non-dimensional elastohydrodynamical number $\mathcal{N}$: experimental data (same symbols as in figure 3) and theoretical curves from the potential flow model (—) and from the momentum conservation model (- - -).

sheets C_d appears to decay with $\mathcal{N}$. Here also, both theories are seen to qualitatively describe the evolution of the drag coefficient. The theoretical values deduced from the potential flow model underestimate the experimental data in the whole $\mathcal{N}$ range investigated and the difference between the data sets is small at high $\mathcal{N}$. Finally note that the astonishing quantitative agreement of the theoretical values obtained by the momentum conservation model with the experiments must be ascribed to the arbitrary choice of the section as adjustement parameter.

4.4. *The limit of large elastohydrodynamical number*

As the elastohydrodynamical number becomes large (fast flow or very flexible sheet), the cone becomes sharp and $\epsilon = \pi/2 - \alpha$ approaches 0. In general, the pressure field should vanish as well for $\epsilon = 0$, so that we expect $\tilde{P} \sim \epsilon^a$, with $a > 0$. In the case of the two models used here, $\tilde{P} \sim \epsilon^2$ so that the equilibrium condition and the drag coefficient definition yield

$$\epsilon = \pi/2 - \alpha \sim \mathcal{N}^{-1/6} \quad \text{and} \quad C_d \sim \mathcal{N}^{-2/3}. \tag{4.5}$$

These scalings account for the slow increase of the equilibrium angle α and the faster decrease of the drag coefficient C_d with the elastohydrodynamical number $\mathcal{N}$. However this limit is not reached experimentally: the sheet loses axisymmetry, probably owing to friction between different layers. The scaling for the drag is the same in the two-dimensional case (Alben *et al.* 2002, 2004), although the scaling for the shape is different ($\epsilon \sim \mathcal{N}^{-1/3}$).

5. Concluding discussion

When subjected to the load of a fluid flow, a circular sheet cut along a radius reconfigures into a cone. We have showed that this behaviour, previously observed for broad leaves in high wind, is mainly due to the mechanical equilibrium of the sheet and is controlled by the non-dimensional elastohydrodynamical number $\mathcal{N}$ (3.4) which measures the balance between flow pressure and sheet bending rigidity. Comparison

https://doi.org/10.1017/S0022112006000851 Published online by Cambridge University Press

with the drag on a rigid circular sheet shows that the sheet deformation allows a substantial drag reduction. A model that couples hydrodynamics and elasticity was derived. Its main limitation is in the computation of the pressure field. Resorting to full numerical simulations might be useful to refine the present study. In spite of its limitations, the model semi-quantitatively accounts for the cone becoming sharper and for the drag reduction as the fluid velocity is increased.

Returning to the reconfiguration of leaves, our system has two main simplifications. On the one hand, leaves are stiffened by their veins. However, in tree leaves, the stiffer (and older) veins often bifurcate from the same point (the end of the petiole), which allows folding into a cone without deforming these veins. On the other hand, the geometry of a leave is more akin to that of a sector of disk of opening angle $\beta < 2\pi$ which cannot fold into a cone of angle less than $\alpha = \cos^{-1}(\beta/2\pi)$, so that we expect a threshold for reconfiguration. Also, using the values of the bending rigidity D in the range 5×10^{-5} to 5×10^{-3} N m (Read & Sanson 2003, for thick leaves), an airflow of velocity $U = 10\,\mathrm{m\,s^{-1}}$ and a size R in the range 5–10 cm, the elastohydrodynamical number $\mathcal{N}$ is found to be in the range 5–500. As a consequence, only some types of leaves would be subject to reconfiguration above a threshold in wind velocity, in agreement with observations. To summarize, our results should hold qualitatively for the reconfiguration of leaves and yield a first step in the full understanding of the drag reduction in trees.

We thank Benoît Roman, José Bico and Médéric Argentina for suggestions and discussions. This article has greatly benefited from the input and the corrections of Emmanuel de Langre to whom we are very grateful.

REFERENCES

Alben, S., Shelley, M. & Zhang, J. 2002 Drag reduction through self-similar bending of a flexible body. *Nature* **420**, 479–481.

Alben, S., Shelley, M. & Zhang, J. 2004 How flexibility induces streamlining in a two-dimensional flow. *Phys. Fluids* **16**, 1694–1713.

Etienne, S. & Pelletier, D. 2005 A general approach to sensitivity analysis of fluid-structure interactions. *J. Fluids Struct.* **21**, 169–186.

Hoerner, S. F. 1993 *Fluid-dynamic Drag*. Bakersfield, CA: Hoerner Fluid Dynamics.

Howe, M. S. 1998 *Acoustics of Fluid-Structure Interactions*. Cambridge University Press.

Landau, L. & Lifchitz, E. 1990 *Théorie de l'Élasticité*. Moscou: Mir.

Lorillu, O., Weber, R. & Hureau, J. 2002 Numerical and experimental analysis of two-dimensional separated flows over a flexible sail. *J. Fluid Mech.* **466**, 319–341.

Niklas, K. J. 1999 A mechanical perspective on foliage leaf form and function. *New Phytol.* **143**, 19–31.

Rayleigh, Lord 1945 *The Theory of Sound*, 2nd Edn, Vol. I. Dover.

Read, J. & Sanson, G. D. 2003 Characterizing sclerophylly: the mechanical properties of a diverse range of leaf types. *New Phytol.* **160**, 81–99.

Schouveiler, L., Eloy, C. & Le Gal, P. 2005 Flow-induced vibrations of high mass ratio flexible filaments freely hanging in a flow. *Phys. Fluids* **17**, 047104.

Vogel, S. 1989 Drag and reconfiguration of broad leaves in high winds. *J. Expl Bot.* **40**, 941–948.

https://doi.org/10.1017/S0022112006000851 Published online by Cambridge University Press